Algorithmic Localisation of Noise Sources in the Tip Region of a Low-Speed Axial Flow Fan

Bence Tóth[1], János Vad

Department of Fluid Mechanics, Faculty of Mechanical Engineering, Budapest University of Technology and Economics. Bertalan Lajos street 4-6., H-1111 Budapest, Hungary.

Abstract

An objective and algorithmised methodology is proposed to analyse beamform data obtained for axial fans. Its application is demonstrated in a case study regarding the tip region of a low-speed cooling fan. First, beamforming is carried out in a co-rotating frame of reference. Then, a distribution of source strength is extracted along the circumference of the rotor at the blade tip radius in each analysed third-octave band. The circumferential distributions are expanded into Fourier series, which allows for filtering out the effects of perturbations, on the basis of an objective criterion. The remaining Fourier components are then considered as base sources to determine the blade-passage-periodic flow mechanisms responsible for the broadband noise. Based on their frequency and angular location, the base sources are grouped together. This is done using the fuzzy c-means clustering method to allow the overlap of the source mechanisms. The number of clusters is determined in a validity analysis. Finally, the obtained clusters are assigned to source mechanisms based on the literature. Thus, turbulent boundary layer – trailing edge interaction noise, tip leakage flow noise, and double leakage flow noise are identified.

Keywords: axial flow fan, fan noise, beamforming, broadband noise, Fourier analysis, fuzzy clustering

Email addresses: tothbence@ara.bme.hu (Bence Tóth), vad@ara.bme.hu (János Vad)
[1]Corresponding author.

Nomenclature

Latin letters

a	dimensionless amplitude of Fourier component
B	number of fan blades
c	number of fuzzy clusters
C	blade chord length
d	diameter
D	Lieblein diffusion factor
f	frequency
G	gradient of source intensity level drop
h	harmonic wave number
l	dimensionless filtering threshold
m	fuzzifier
Ma	Mach number based on W
n	circumferential wave number
N	number of all points to cluster
$\mathbb{N}$	the set of natural numbers
P	sound pressure
p	dimensionless sound pressure
Re	Reynolds number based on C and W
S_b	blade spacing
Str	Strouhal number
t	thickness of blade plate
w	membership value
W	relative flow velocity
Z	source – aperture distance

Greek letters

α	flow angle of attack
β	angular position of base source
γ	stagger angle (measured from axial direction)
δ	boundary layer thickness
φ	circumferential angle
κ	factor in the resolution criteria
λ	wavelength
$\boldsymbol{\mu}$	cluster centre
τ	tip clearance
θ_c	camber angle of circular arc camber line
Θ	angle between two sources to separate
$\boldsymbol{\xi}$	data point for clustering

Superscripts and subscripts

0	refers to the threshold of hearing
a	aperture
f	third octave band index, referring to the middle frequency
i	index of data points
j	index of clusters
max	maximum
peak	related to source peak
t	tip
opt	optimal

Abbreviations

FCM	Fuzzy c-means clustering
LE	Leading edge
PAM	Phased array microphone
PSF	Point spread function
ROSI	Rotating Source Identifier
SPL	Sound pressure level
SSL	Source strength level
TBL	Turbulent boundary layer
TE	Trailing edge
XB	Xie-Beni index

1. Introduction

Noise reduction is a focal point in research related to low-speed axial flow fans. Because of the large numbers of such devices and their role in everyday life, their noise is to be reduced, in order to improve human life quality and consumer satisfaction.

To achieve this goal, noise generation mechanisms are to be understood and controlled. Noise sources are to be localised, their strengths compared, and connected to the phenomena that cause them. Correlations between aerodynamic and noise source properties are to be determined, serving as a basis for design guidelines, such as in [1]. Then, by modifying the geometry, the fan designer aims at reducing noise and aerodynamic loss at prescribed aerodynamic performance (flow rate and total pressure rise). In order to obtain the aforementioned correlations, the noise sources are to be investigated. The present paper is focused solely on broadband noise sources.

Acoustic beamforming, relying on a phased array microphone (PAM) measuring technique, is an effective tool for noise source localisation [2, 3]. It is based on processing simultaneously sampled microphone signals. The method can be extended to localise sources in rotating systems [4, 5, 6]. In the present investigation, the Rotating Source Identifier (ROSI) [4] method is applied, providing

beamform results characterising the locations and strengths of noise sources related to the rotating fan blades [7, 8, 9, 10].

The results of beamforming are often represented visually as beamform maps. The interpretation of such maps requires experience and involves subjective and arbitrary elements. This is partly due to the complexity of the noise generation phenomena, and partly to the uncertainty incorporated in the beamforming method itself. This means the following difficulties.

- Beamform maps contain sidelobes. These are false source locations that result from partial coherence of the recorded pressure signals at locations being different from those of the true sources [2]. Due to these sidelobes, non-physical, false peaks appear on the beamform maps. Furthermore, even the physically meaningful peaks may have values falsified by sidelobe effects.

- In some cases, uncertainty is present in determining the radial position of rotating sound sources [11, 12].

- If an extended region of intense noise appears, its evaluation is charged with uncertainty, due to the limitation in the spatial resolving power of the beamforming technique. It may be the manifestation either of multiple small-scale sources being close to each other, or the manifestation of a single but spatially extended source.

The issue of the last point, related to the spatial resolution of the technique, is often attempted to be tackled with use of optics-based resolution criteria [8, 13, 14, 15]. These were historically established for human vision, and therefore, their application is dubious in acoustic beamforming. Some of such criteria are the Rayleigh, the Dawes, and the Sparrow limit [16]. These criteria can all be given in the form of Eq. (1), with only the factor κ varying.

$$\sin\Theta = \kappa\frac{\lambda}{d_a} \tag{1}$$

Here d_a is the diameter of circular the optical aperture, λ is the wavelength and Θ is the smallest viewing angle at which two sources can be separated. In case of microphone arrays, the aperture size is usually taken as the diameter of circumscribed circle of the array [14].

Mathematically, the criteria and the κ factors are based on the point spread functions (PSF) of the sources. The different κ values were historically introduced in optics as subjective and arbitrary criteria, partly depending on the resolving power of the eye of the observer. When a point source located at infinite distance emits light that is observed through a circular aperture, an image is formed, the intensity distribution of which is described by means of the PSF. When two point sources of identical strength are observed, the resultant image pattern depends on the separation between the sources. Between the two intensity peaks of the two PSFs, a "dip", i.e. intensity decrease, occurs. Such dip is expressed as the percentage of the peak intensity. The Rayleigh, Dawes and Sparrow limits define the resolving power based on the magnitude of the dip.

The PSFs of the two incoherent point sources, their sum and the dip are illustrated in Fig. 1.

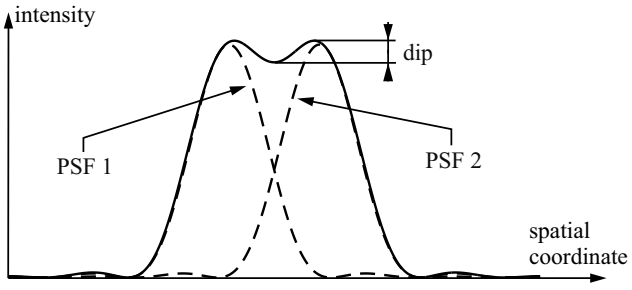

Figure 1: PSFs (dashed), their sum (solid), and the dip

Table 1, based on [16], presents how κ and the dip vary for the various optics-based limits. These are arbitrarily derived from - and, as such, are restricted to - two neighbouring PSFs described using first order Bessel functions [17]. The 0 % dip - i.e. a central plateau - obtained for the Sparrow limit means that

the two neighbouring sources cannot be distinguished solely on the basis of the intensity distribution along the line connecting the source centres. They can be distinguished only on the basis of inspecting the full resultant pattern of the two additive PSFs. This points to the fact that the Sparrow limit cannot be applied when the sources are to be distinguished along a line, such as the tip circumference in the present case study.

Criterion	κ	Dip
Rayleigh	1.22	26.5%
Dawes	1.03	5%
Sparrow	0.96	0%

Table 1: κ factors and dip magnitudes for different optics-based resolution criteria

In evaluation of beamform maps, involving subjectivity (visual inspection), the arbitrary use of the Rayleigh limit [8, 13, 14], as well as the Sparrow limit [13, 15] is widespread. The application of the Rayleigh criterion and the Full Width at Half Maximum criterion is investigated in [18], where alternative limits are also introduced.

Besides the subjectivity included in the choice of the criterion, the reliability of application of optics-based criteria in estimating the resolution of beamform maps is also questioned by the following facts (conf. [17]).

a) The criteria were formulated for the case of two point sources of identical strength. However, in general, a priori knowledge is available neither on the point-like feature nor on the strength identity of the sources.

b) The criteria were originally formulated for a circular aperture, for which the PSF is the Airy diffraction pattern [17]. In case of conventional beamforming with microphone arrays, however, the PSF is influenced by the positions of the microphones [2], and, as such, will usually be different from the Airy pattern. In the present study, the microphones are arranged along logarithmic spiral arms, therefore the assumption of a circular aperture is unsubstantiated.

c) As the criteria rely on the Fraunhofer diffraction, the source shall be infinitely far away from the observer. This means that the incoming waves should be plane waves. In fan noise investigations however, the distance between the fan and the array is often confined to the order of magnitude of the rotor tip diameter. In [8], serving as a basis for the present investigation, the array was installed approximately 2 d_t tip diameters away from the fan inlet, while the size of the array is approximately 3 d_t. With such a geometrical configuration, the validity of the plane wave approximation is doubtful, similarly to the case in [15].

In the above overview, the difficulties in evaluating the beamform maps have been outlined. Furthermore, it has been pointed out that the optics-based resolution criteria contain subjective and arbitrary elements, and their assumptions are generally not fulfilled in the context of the PAM technique.

The aim of this paper is to propose a method for processing the beamform maps, quantifying and localising dominant broadband noise sources in axial fans, while overcoming the aforementioned difficulties in processing.

The advantages of the method are the following. It is algorithmic, and avoids the use of subjective judgement, such as visual inspection, and arbitrary elements, such as the choice of resolution criteria. It allows for the concerted evaluation of different third-octave bands simultaneously. It includes filtering, and enhances the periodic sources, by removing perturbations. The method is robust, providing the same results for varied processing parameters. It is able to identify and quantify the sources in a straightforward manner, without a priori knowledge on them. The results are given in terms of the angular locations, frequencies and magnitudes of the significant noise sources.

Preliminary studies to this method are reported in [19, 20]. The application of the method is presented through a case study of an axial flow ventilation fan, the upstream-radiated noise of which has been subjected to PAM investigation.

A localised aeroacoustic source is defined herein as a cluster of base noise sources correlating a) in space, characterised herein by the angular position β

at the fixed radius, and b) in frequency f. Each localised aeroacoustic source of spatially correlating base sources will be assigned to a spatially coherent, organised flow structure, termed herein as *flow phenomenon*. A flow phenomenon is defined herein as the multitude of spatially correlating elementary components of turbulent flow. It is temporally stable, i.e. steady or periodic, in terms of Reynolds averaging of the turbulent flow characteristics. Flow phenomena may interact and influence each other. The co-existing flow phenomena represent a superposition of the related noise mechanisms. Based on references [21, 22, 23, 24, 25, 26], the following traditionally known classes of rotor aeroacoustic noise are considered herein for the near-tip region of an axial fan, assigned to flow phenomena. The denomination of the flow phenomenon in point is written italicized. The noise sources are listed in the sequence of their anticipated approximate location, moving from the blade leading edge (LE) toward the downstream direction.

a) *Near-LE turbulence ingestion* noise. It originates from the impingement of upstream turbulence. The source locates in the vicinity of the LE, in aerodynamically non-compact cases (i.e. if the length scale of upstream turbulence is relatively small in comparison to the blade chord length).

b) *Turbulent boundary layer (TBL)* noise. It originates from the wall pressure fluctuation due to boundary layer turbulence. It radiates over the entirety of the TBL.

c) *Separated flow* noise. It originates from pronounced unsteadiness of flow due to boundary layer separation. For deep stall, the noise radiates from the entirety of the chord. For moderate separation, it dominates near the trailing edge (TE).

d) *Profile vortex-shedding* noise. It originates from coherent vortex shedding over the blade profile. The source extends from the wake toward the region upstream of the TE, within the thickened / separated / reattached boundary layer.

e) *TBL – TE interaction* noise. It is due to the scattering of turbulence in an

attached boundary layer, at the TE, as sound. The source locates in the vicinity of the TE.

f) *Tip leakage flow* noise. It originates predominantly from the passage of tip leakage flow turbulence over the TE of the blade tip region. The source locates in the vicinity of the TE.

g) *Blunt TE vortex-shedding* noise. It originates from coherent vortex shedding from the blunt TE. The source locates close downstream of the TE.

2. Case Study

An axial flow industrial cooling fan was chosen to illustrate the capabilities of the method proposed herein. A sketch of the fan is shown in Fig. 2. Its properties as well as details of the instrumentation, data acquisition and processing are available in [8, 9, 10], therefore only the most representative features are summarised herein. The fan is a free-inlet, free-exhaust rotor-only configuration, built into a short duct with a short inlet cone. The rotor has $B = 5$ blades, tip diameter of $d_t = 0.30$ m and hub-to-tip diameter ratio of 0.3. The rotor speed is 1430 RPM, while the tip gap size is 7 mm. The cambered plate blades are of circular arc camber line, with rounded LEs and TEs, and rounded blade tip. The geometrical data and aerodynamic conditions of the rotor cascade at the tip will be discussed in detail in the Results and Discussion section.

An optical transducer was used to measure the angular position of the rotor, being necessary for the ROSI algorithm. The pressure signals were recorded using an OptiNav, Inc. Array 24 PAM system, and the accompanying processing equipment, i.e. an amplifier, an analogue-to-digital converter, and a laptop computer. The PAM system has 24 omnidirectional microphones, arranged along logarithmic spiral arms in order to suppress sidelobes. The array plate has an octagonal shape, with the diameter of the circumscribed circle being 1 m. It was placed perpendicularly to the rotation axis of the fan on the suction side. The centre of the array coincided with the rotor axis. The array was installed at a distance of $1.83\,d_t$ from the inlet plane of the fan casing. Preparatory

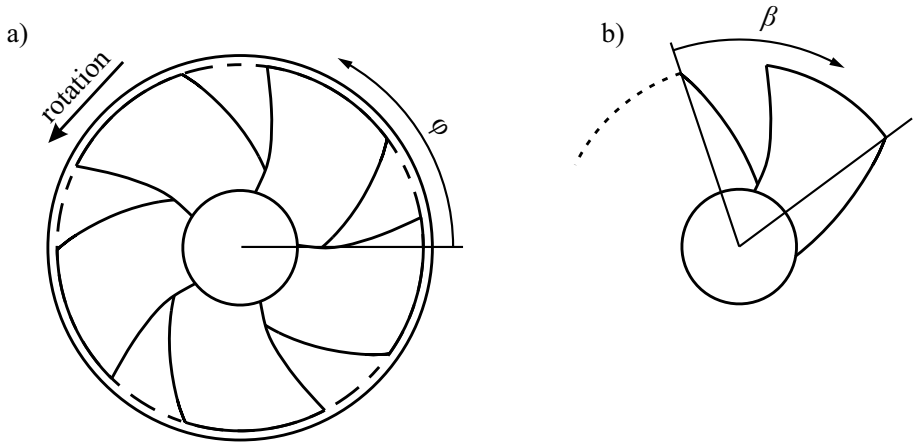

Figure 2: a) Sketch of the fan. b) Interpretation of angle β

measurements carried out by means of a vane anemometer revealed that the impact of the array on the flow field inlet to the fan is negligible. Sampling frequency was set to 44.1 kHz, and data was acquired for 20 s, meaning a total of about 460 revolutions, or 2300 blade passages. In earlier investigations, this averaging time was found adequate from a statistical point of view [10]. The measurements were carried out in a laboratory environment with no special acoustical treatment.

Because the array has no rotational symmetry, frequency domain deconvolution methods, succesfully applied in other investigations [5, 15, 27, 28], were not applicable. Therefore the acquired acoustic data was processed using the ROSI algorithm. This allows the obtainment of beamform maps in a co-rotating frame of reference, by removing the effects of the rotary motion in time domain. Then the cross-spectral matrix has been calculated by averaging the cross-spectra of blocks with 1024 samples, windowed by a von Hann function, with 50% overlap. About 1700 windows were averaged in total. To remove the effects of uncorrelated noise, the main diagonal of the cross spectral matrix has been removed. Due to the general arrangement of the microphones, deconvolution methods were not available, therefore conventional frequency-domain beamforming has been applied. The same procedure was repeated for each point of the beamform

grid, thus narrowband source strength level (SSL) distributions were obtained. SSL is the output of the beamforming process, e.g. Eq. (2.29) in reference [2], written in a level form. Based on reports on comparable measurement configurations [5, 15], microphone directivity effects were neglected.

The beamforming computations were carried out in the third-octave bands with central frequencies between 2 kHz and 6.3 kHz. The reason for omitting the bands below 2 kHz is the limitation in the spatial resolution of the beamforming process.

The narrowband sound pressure level (SPL) spectrum recorded by the microphone being the closest to the array centre is shown in Fig. 3 in the 20 Hz – 20 kHz range. As the figure shows, there are no significant tonal components in the 2 kHz – 6.3 kHz range. Even out of this range, no outstanding tonal peaks are dominant, neither at the blade passing frequency at 119 Hz. It can be concluded that the noise is of broadband origin. Therefore the appropriate narrowband results were summed, and third-octave band beamform maps were generated, centred on 2000 Hz, 2500 Hz, 3150 Hz, 4000 Hz, 5000 Hz, and 6300 Hz.

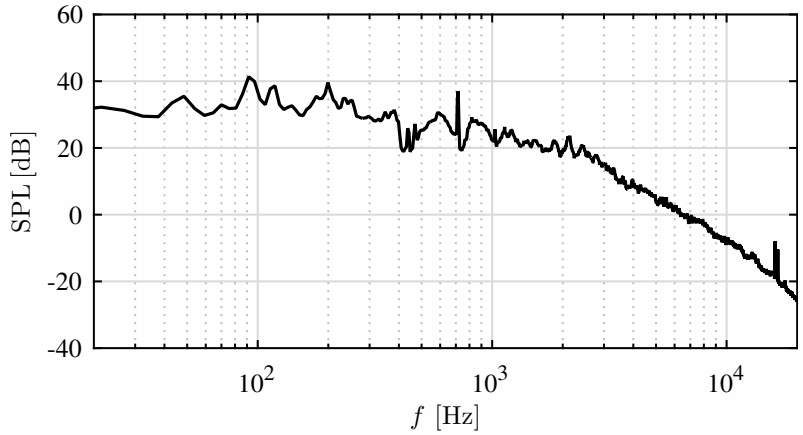

Figure 3: Noise SPL spectrum recorded by a single microphone. Frequency resolution: 5.8 Hz

The third-octave band beamform maps are shown in Fig. 4, reproduced from [9]. The figures indicate the SSL in each third-octave band. In this view, the

fan rotates in the counter-clockwise direction. The figures show a 5 dB dynamic range. The details of noise patterns below the lower limit of the dynamic range have been discarded.

By visual inspection of Fig. 4, the blade-passage-periodicity of the noise pattern is apparent. As the frequency increases, more and more details can be observed. Generally, only a single source per blade passage can be seen, however, the highest frequency maps suggest the presence of multiple sources. Nevertheless, their exact number cannot be determined by visual means.

The visual interpretation highlights the evaluation problems discussed in the Introduction. The beamform maps can only be evaluated in a piecewise manner, i.e. each frequency band separately, through visual inspection. The data processing and evaluation algorithm presented herein incorporates each frequency band in a concerted manner. The method is based on Fourier analysis, supplemented with fuzzy clustering.

3. The Proposed Method

3.1. Data extraction

For further data processing, an angular distribution of SSL, obtained from the beamforming process, has been extracted from each beamform map. This means taking the SSL at a given radius as a function of a circumferential angle $\varphi \in [0, 2\pi)$, shown in Fig. 2.

The extraction can be carried out for any radius of the maps. For the present purpose of illustrating the capability of the data processing method, the tip radius of the fan, $d_t/2 = 0.15$ m has been chosen. The reason for this choice is that the blade tip region exhibits a remarkable circumferential variation in both aerodynamic and aeroacoustic features, as shown in e.g. in [15], and, as such, it is expected to give illustrative results.

$\mathrm{SSL}_f(\varphi)$ distributions have been extracted for each third-octave band under processing. An analogy is considered between SSL and SPL. On this basis, SSL is used to define the dimensionless effective sound pressure p. p is taken as $p =$

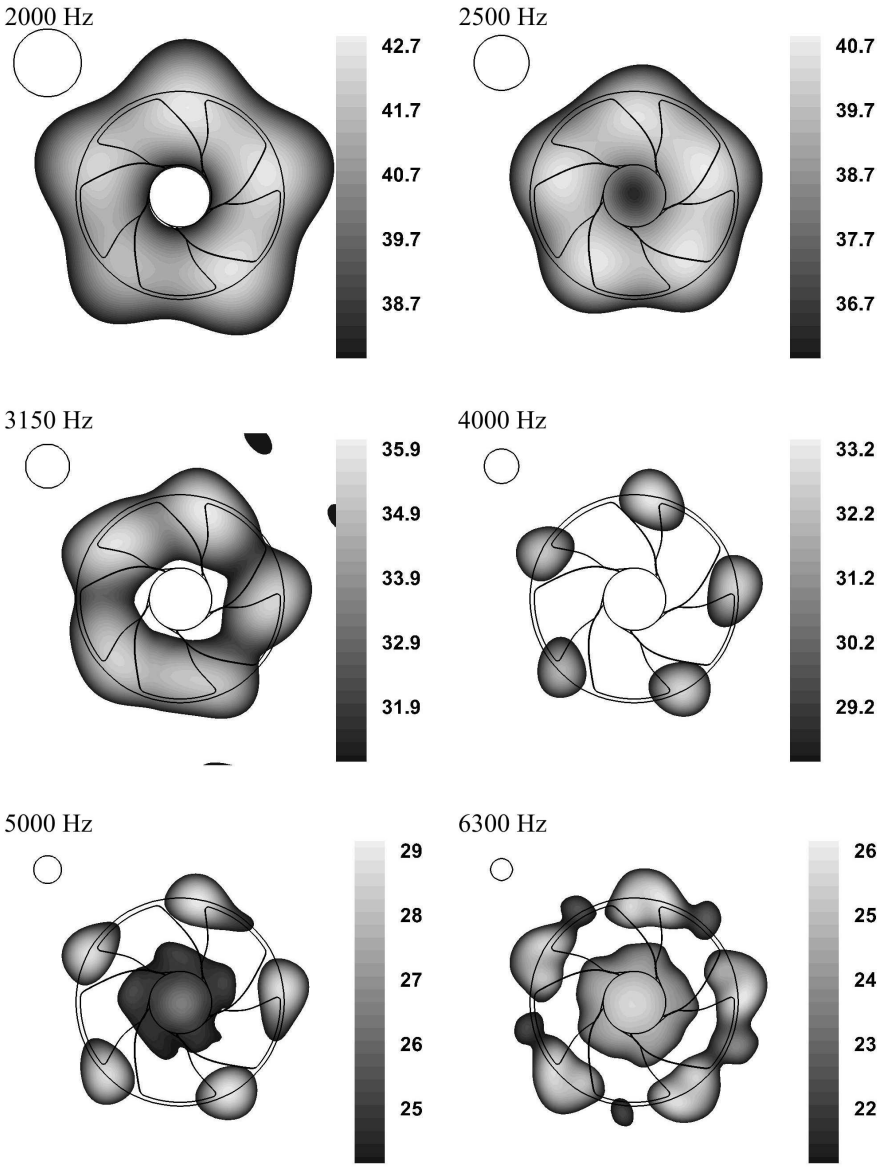

Figure 4: Beamform maps for each investigated third-octave band, reproduced from [9]. The labels indicate the third-octave band mid-frequencies, the solid circles show the casing, while the contours show the SSL [dB]. The rotor rotates in the counter-clockwise direction. Circles in the top-left corner indicate the Rayleigh resolution limit at the centre frequency, calculated as $Z \sin \Theta$ using Eq. (1) on the basis of [14].

P/P_0. P is the fictitious effective sound pressure obtained from beamforming. $P_0 = 2 \cdot 10^{-5}$ Pa is the threshold of hearing. The following relationship is valid:

$$\mathrm{SSL}_f(\varphi) = 20 \log \frac{P_f(\varphi)}{P_0} = 20 \log p_f(\varphi) \tag{2}$$

In what follows, the $p_f(\varphi)$ dimensionless pressure is used for the purposes of the analysis, obtained from the SSL beamform maps, using Eq. (2). Its distributions for the various third-octave bands are shown later in Fig. 6 with solid lines.

3.2. Fourier decomposition and filtering

The present work aims at contributing to the empirical background of concerted aerodynamic-aeroacoustic design of axial fan *rotor blade cascades* of low noise emission. Therefore, the beamform results are intended to be exploited as follows. Those broadband aeroacoustic sources are to be localised, which are assigned to the blade passages being ideally of periodically repetitive geometrical and flow conditions - as treated in the rotor blade cascade design approach. The blade-passage-periodic acoustic sources are the exclusive subjects of the present survey. Blade-passage-periodicity means that a source is present for each blade passage with identical source strength distribution in space and in frequency. Each source is considered as a composition of blade-passage-periodic *base sources*. With consideration of the number of blades B, the base sources periodically repeat themselves along the entire circumference B times as well its integer multiples. The effects violating blade-passage-periodicity are untreatable by classic rotor cascade design means. Therefore, they are considered herein as perturbations, and are arbitrarily excluded, i.e. filtered out, from source localisation. The causes of such perturbations are classified as follows, together with some examples.

a) *Irregularities of inlet flow condition.* Asymmetric mean velocity field, due to distortions in the upstream geometry. Randomly ingested, stretched, large-scale eddies, due to upstream flow obstacles.

b) *Non-periodicity of geometrical boundaries of the blade passages, due to manufacturing or assembling imperfections, or deformations.* Non-uniform tip clearance along the circumference, due to the eccentricity of the rotor inside the casing. It represents 1 perturbation period along the entire circumference. Blade(s) of geometry being different from that of the regular blade set - e.g. different span, stagger, or profile geometry -, leading to a local modification of the emitted noise. The number of irregular blade(s) correspond to the same number of perturbation periods along the circumference.

c) *Non-periodicity of blade passage flow, unsteadiness in the Reynolds averaged flow quantities.* Rotating stall.

d) *Perturbations caused by the acoustic environment.* Background noise, with non-uniform features.

e) *Perturbations caused by measurement and processing uncertainties.* Sidelobes resulting from the beamforming algorithm that are non-periodic along the circumference within a rotation.

The wave-like intensity patterns in Fig. 1 suggest that a combination of cosine functions is a reasonable approximate representation for a single source, or for interacting neighbouring sources. Together with the required blade-passage-periodicity, these two suggest the application of Fourier analysis.

The $p_f(\varphi)$ angular distributions in each third-octave band are expanded into Fourier series as expressed in Eq. (3).

$$p_f(\varphi) = \sum_{n=0}^{n_{\max}} a_f[n] \cos\left(n\left(\varphi - \beta_f[n]\right)\right) \tag{3}$$

Thus, each distribution is expressed as a sum of cosine functions with amplitude a_f and angle β_f depending on the discrete n circumferential wave number.

Blade-passage-periodic sources are represented by the Fourier components of $n = B$ as well as their physically relevant harmonics. Only those are to be retained for further processing. The formerly listed perturbations, characterised by m values being different from those for the blade-passage-periodic components, are to be filtered out.

The harmonic wave number h is introduced in Eq. (4). Using this definition, for a positive integer h, the value of $a_f[h]$ is interpreted as the amplitude of a mode that has exactly h periods in one blade passage, while $h = 0$ means the circumferential average value.

$$h = n/B \tag{4}$$

An illustrative amplitude spectrum as a function of the harmonic wave number, $a[h]$, is shown in Fig. 5.

The aim of the investigation is to identify the significant blade-passage-periodic components that are related to physical aeroacoustic/aerodynamic phenomena. These are expected to have a periodicity around the circumference, corresponding to that of the blades, and to appear once ($h = 1$), twice, etc. (harmonics, $h = 2, 3...$) per blade passage. Thus the positive integer h values are to be investigated. Components of other, non-integer harmonic wave numbers are considered as perturbation. The previously mentioned rotor eccentricity for example will cause a peak at the harmonic wave number corresponding to the reciprocal of the blade number, $h = 1/B$, while irregularities in the blades will appear at the reciprocal of the number of the irregular blades. All of the aforementioned effects may cause perturbation at their harmonics, too.

Therefore, only the physically relevant - "significant" - Fourier components associated with integer h values are to be retained for further processing. At this point, a criterion is necessary to determine which of these components is to be judged "significant". The following criterion is proposed. Within a given third-octave band, a component at an integer h is judged significant only if its amplitude exceeds the amplitude of the maximum perturbation component, e.g. the maximum of the spatial spectrum that is found at a fractional h. In other words, a significant peak has an amplitude larger than the limit in that frequency band, see Eq. (5).

$$a_f[h] > l_f \tag{5}$$

Here the limit is the maximum perturbation amplitude, that is, the highest amplitude found at a fractional h, as described in Eq. (6).

$$l_f = \max_{h \notin \mathbb{N}} \; a_f[h] \tag{6}$$

Here $\mathbb{N}$ denotes the set of natural numbers (including 0).

As an example, a resultant spectrum is shown in Fig. 5 for the third-octave band centred on 6300 Hz. The filtering threshold, determined as the maximum perturbation amplitude being present at $h = 3/5$, is indicated in the figure with a horizontal dashed line. When applying the inequality in Eq. (5) in selecting the significant peaks, it is to be considered that the maximum perturbation amplitude has an error due to the amplitude uncertainty of the PAM technique (as reported e.g. in [8]). A peak is judged to be significant if it is higher than the maximum perturbation amplitude plus the half-width of the range of PAM amplitude uncertainty. This choice guarantees that each component of the blade-passage-periodic sources (at $h = 1, 2, 3, \ldots h_{\max}$) exceeding the filtering threshold, i.e. being more significant than the perturbations, is considered in the identified sources.

Regarding Fig. 5, it is noted that, besides the significant components at $h = 1$ and $h = 3$, a significant component is also present at $h = 0$, corresponding to the circumferential average of the beamforming data under discussion.

Using the decomposition and filtering technique, the source strength around the blade tip can be represented in a simplified manner. First, only the significant components are kept, and then, the distribution can be represented by just the amplitude, harmonic wave number, and phase angle of those significant components. Figure 6 presents the circumferential distributions reconstructed from only the significant base sources with dashed lines. The agreement between the originally measured and the reconstructed distributions is fair.

By choosing the Fourier analysis as a processing technique, cosine functions are chosen for characterising the circumferential variation in the intensity of the base sources. When reconstructing the original distributions in Fig. 6, the

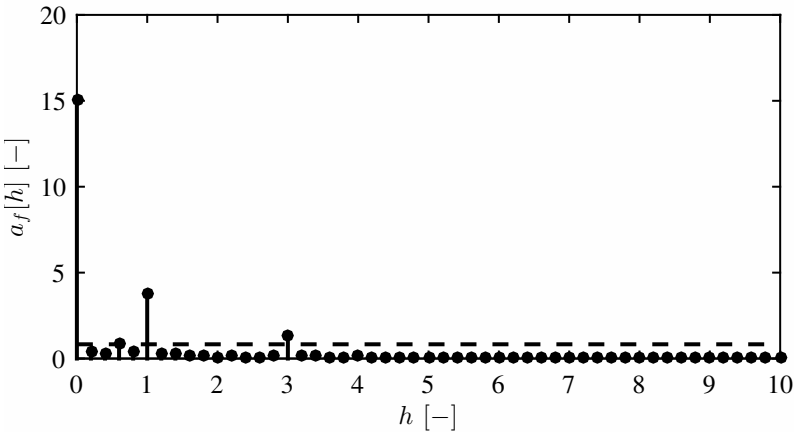

Figure 5: Spatial spectrum with the filtering threshold (horizontal dashed line) in the third-octave band centred on 6300 Hz

circumferential average values (related to $h = 0$) as well as the cosinusoidal base sources are applied. The applied process enhances the detectability of the blade-passage-periodic sources, as perturbations at fractional h values are excluded from further processing.

The good reconstruction shows that the method captures the most significant blade-passage-periodic aeroacoustic phenomena, even if only a few components are used. The base sources retained after filtering are listed in Table 2. Here the component ID consists of the third-octave band mid-frequency, then the h value, then an ordinal number going from 1 to h identifying each component.

The subject of future work is the investigation of the performance of the presented filtering method throughout the whole annulus area.

Table 3 shows the circumferential average values, the threshold limits, and the percentage of the latter to the former. The percentages in the last column show that the filtering method is able to capture fine oscillations. The percentages are significantly below the half-value of the dip for the Rayleigh criterion, being 13%, according to Table 3. This means that the Rayleigh criterion is overly conservative, and the presented method is able to extract fine details even below the Rayleigh limit.

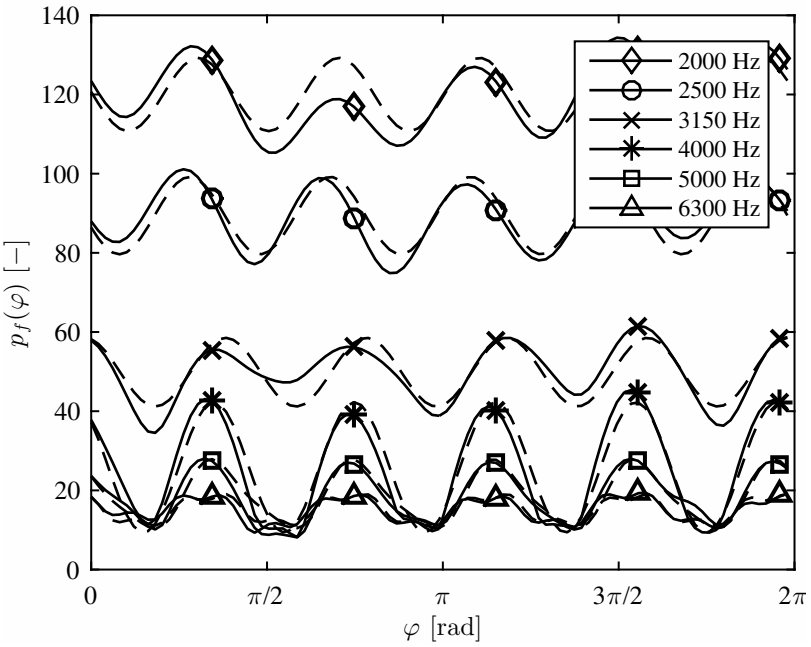

Figure 6: Distributions of $p_f(\varphi)$ along the circumference: measured (solid) and reconstructed after filtering using the significant components only (dashed)

Component ID	Cluster assigned	a_f [−]	β [°]
2000 / 0	—	120.00	—
2000 / 1 / 1	1	9.26	14.9
2500 / 0	—	89.42	—
2500 / 1 / 1	1	9.78	10.5
3150 / 0	—	49.86	—
3150 / 1 / 1	1	8.68	28.9
4000 / 0	—	25.83	—
4000 / 1 / 1	1, 2	16.45	22.8
5000 / 0	—	18.52	—
5000 / 1 / 1	2	8.23	24.1
5000 / 2 / 1	2	1.69	18.0
5000 / 2 / 2	3	1.69	54.0
6300 / 0	—	15.08	—
6300 / 1 / 1	2	3.74	20.8
6300 / 3 / 1	2	1.32	7.0
6300 / 3 / 2	2	1.32	31.0
6300 / 3 / 3	3	1.32	55.0

Table 2: Base sources

Figure 7 shows the maximum SSL spectrum, i.e. the maximum SSL values in the tip region in each beamform map. The tip region is defined as those d diameters where $\frac{|d-d_t|}{d_t} < 0.05$. The figure confirms that the noise has broadband characteristics in the investigated frequency range.

The $[\beta, f]$ coordinates for the maxima composing the SSL spectrum are shown in Fig. 8. When creating this figure, the periodicity of the blades was taken into account. As illustrated in Fig. 2, and will be presented later in Fig. 10 as well, the angle β representing the position of a source within a blade passage is zero at the TE, and increases as one moves towards the TE of the adjacent blades, located at $\beta = 360°/B = 70°$.

f [Hz]	$a_f[0]$ [−]	l_f [−]	$l_f/a_f[0]$ [%]
2000	120.00	6.08	5.07
2500	89.42	2.70	3.02
3150	49.86	2.33	4.66
4000	25.83	2.64	10.22
5000	18.52	1.32	7.13
6300	15.08	0.83	5.50

Table 3: Resolution thresholds

Fig 8 suggests that the elementary narrowband sources form "clusters" over the $[\beta, f]$ plane. This observation inspires the concept of clustering for the base sources in Table 2.

3.3. Clustering

The peaks of the cosine-shaped significant Fourier components are considered as base sources. A Fourier component characterised by a harmonic wave number h originates base sources in number of h per blade passage. These base sources are to be clustered for identification of the physically distinct noise sources.

The aspects of clustering are the spatial location, characterised by angle β, and the frequency f. β is included, because base sources originating from the same source mechanism are expected to be located close to each other. f is used, because broadband sources are investigated, which have continuous amplitude distributions as a function of frequency. The clustering method was chosen considering that the clusters can overlap in both spatial location and frequency range.

Based on these arguments, clustering was carried out in the [β, f] plane for the significant peaks identified by the filtering process. The number of significant elements to cluster is the number of terms in Table 2 with $h > 0$, $N = 11$.

The $\boldsymbol{\xi}_i$ data points contain the angular location and the frequency of the

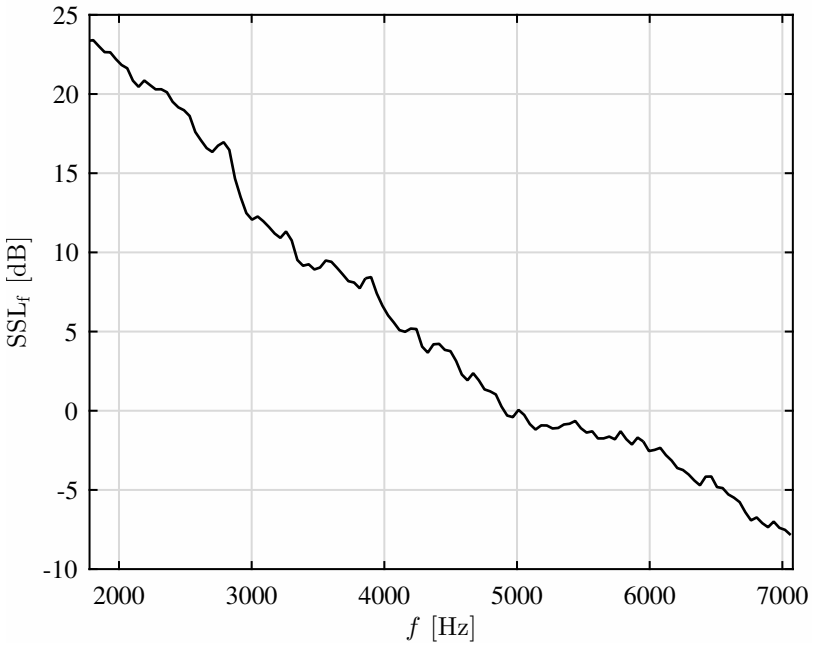

Figure 7: Maximum SSL values in the tip region. Frequency resolution: 43.1 Hz

base source (see Eq. (7)).

$$\boldsymbol{\xi_i} = \left[\hat{\beta}_i,\ \hat{f}_i\right] \tag{7}$$

A widely applied method is the Fuzzy c-means Clustering (FCM) [29]. It creates a predefined c number of clusters based on the $\boldsymbol{\xi}_i$, $i = 1 \dots N$ data points. This is achieved by choosing the $\boldsymbol{\mu}_j$, $j = 1 \dots c$ centres in a way, that the point-to-centre distances are minimised, see Eq. (8). The method is fuzzy, as it contains wi, j membership functions connecting each element to each cluster centre. This way, an overlap between the clusters is allowed, i.e. each data point belongs to each of the c clusters with a certain membership function. These $w_{i,j}$ values quantify how well a data point belongs into a certain cluster, and serve as weights for the element-to-cluster distances. A constraint on the membership functions is that the sum of those for a data point with respect to each cluster

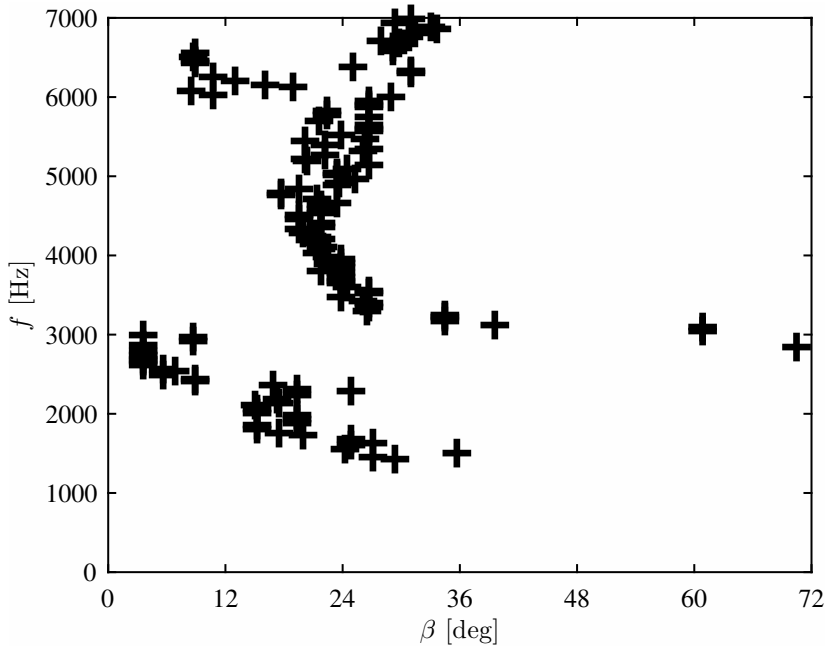

Figure 8: $[\beta, f]$ coordinates for the narrowband maxima, merged into a single blade passage region

is unity, i.e. $\sum_{j=1}^{N} w_{i,j} = 1 \, \forall i$.

$$\arg\min \sum_{i=1}^{N} \sum_{j=1}^{c} w_{i,j}^{m} \, ||\boldsymbol{\xi}_i - \boldsymbol{\mu}_j||^2 \tag{8}$$

The equation contains a parameter m, the so-called fuzzifier. For $m = 1$, crisp (e.g. traditional, non-fuzzy) clusters are obtained, with no overlap between them. On the other hand, as $m \to \infty$, all membership values converge to a uniform value of $1/c$ [29], i.e. the ability to differentiate between clusters diminishes. In absence of any a priori information on choosing the relevant m value, $m = 2$ is usually set [30]. In order to avoid this arbitrary choice, a parameter sensitivity study has been carried out.

The method of calculation is the following. First, $w_{i,j}$ values are initialised randomly. Then, the $\boldsymbol{\mu}_j$ cluster centres are given as the weighted average of the data points (Eq. (9)).

$$\boldsymbol{\mu}_j = \frac{\sum_{i=1}^{N} w_{i,j}^{m} \, \boldsymbol{\xi}_i}{\sum_{i=1}^{N} w_{i,j}^{m}} \tag{9}$$

The membership values are then calculated using Eq. (10). After that, Eqs (9) to (10) are iterated until the change of $w_{i,j}$ values is less than a prescribed criterion.

$$w_{i,j} = \frac{\left(\frac{1}{||\boldsymbol{\xi}_i - \boldsymbol{\mu}_j||^2} \right)^{\frac{1}{m-1}}}{\sum_{k=1}^{c} \left(\frac{1}{||\boldsymbol{\xi}_i - \boldsymbol{\mu}_k||^2} \right)^{\frac{1}{m-1}}} \tag{10}$$

Some applications of the FCM method related to acoustics, fluid mechanics, or processing of measurement data are the following. It has recently been applied for aero-engine failure detection [31], and for the processing of magnetic resonance images to identify different tissue types [32, 33], with special attention on repeatability and objectivity, thus without including human operators. It has been applied to improve source localisation in reverberant environments [34]. In the field of fluid dynamics, the vortex field of an oscillating cylinder has been analysed with clustering after a reduction of dimensions with proper orthogonal

decomposition [35]. Patterns in a turbulent flow have been analysed in [36]. Clustering has furthermore been applied to recognise user-specific sound patterns [37], and detect organic compounds based on sensor array measurements [38].

To the authors' best knowledge, the present application of clustering is the first one in analysing acoustic beamform maps related to rotating fluid machinery.

3.4. Number of clusters

The number of clusters per blade passage, c, has to be set as input data for the clustering algorithm. It has a significant effect on the results, therefore special attention is to be paid to its setting. The appropriate c value may be approximated by visual inspection of the data set, on a trial-and-error basis, but such method involves subjective elements, and, as such, it cannot be algorithmised. Therefore, another approach was implemented that is automatised and objective. Cluster validity indices are calculated, describing how reliable the clustering is, for possible values of c. Then the optimum number of clusters is set based on these validity indices.

There are several cluster validity indices, with many of them summarised in [39]. However, none of them is generally applicable and always reliable [39, 40]. For the present study, the Xie-Beni index (XB) [41], defined in Eq. (11), was chosen as the cluster validity index to be examined. The reason for choosing XB is that it characterises clustering in a way being relevant to the present studies. The numerator quantifies the variation within clusters, which is analogous to the error caused when replacing a data point with the cluster centre. The denominator contains the distance of the two closest cluster centres, thus characterises the separation of the clusters. Since well separated, compact cluster are sought for, XB has an absolute minimum value at the optimum number of clusters. Supporting the choice of XB, references [35, 36] report on clustering

related to fluid dynamics, with effective involvement of XB.

$$\mathrm{XB} = \frac{\sum_{i=1}^{N} \sum_{j=1}^{c} w_{i,j}^{m} \, ||\boldsymbol{\xi}_i - \boldsymbol{\mu}_j||^2}{N \min\limits_{i \neq j} ||\boldsymbol{\mu}_i - \boldsymbol{\mu}_j||^2} \tag{11}$$

From the definition of XB follows that at least two clusters must be present in the data for the proposed algorithm to provide meaningful results.

Figure 9 shows the XB values for different cluster sizes and different m values, inspired by [35, 36], in the present case study. For the first approximation of the maximum number of clusters to be tested, $\sqrt{N}$ is suggested as a rule of thumb [30]. In the present case study, the number of elements to be clustered is the number of the base sources, $N = 11$. For an extended investigation, a value of $c = 5$ (exceeding $\sqrt{11}$, rounded up to 4) was set herein as an upper limit. The minimum of XB indicates the optimum cluster number is $c_{\mathrm{opt}} = 3$, regardless of the choice of the m fuzzifier. Therefore the optimum number of clusters was robustly found at $c_{\mathrm{opt}} = 3$, and clustering was carried out with 3 clusters.

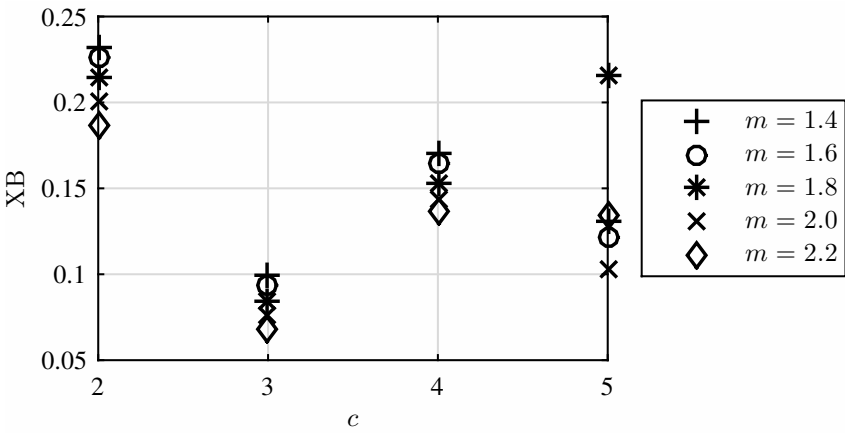

Figure 9: XB index as a function of c for different m values

It has to be taken into account, that the β and f coordinates of the data points (base sources) to be clustered are charged with error. The error of β is due to the uncertainty of the angular encoder. It is estimated conservatively as $\pm 2.5^\circ$ in [10]. The dominant error of f originates from the 1024-point discrete

Fourier transform applied in creating the beamform maps. It is estimated as ± 22 Hz.

It is to be investigated whether the determination of optimum number of clusters is affected by the uncertainty of the $[\beta, f]$ coordinates of the base sources. It has been observed that varying m results in a scatter of the localised cluster centres (not presented herein) pessimistically exceeding the aforementioned uncertainty ranges of β and f. Therefore, the analysis of m-sensitivity of locating the cluster centres is an implicit representation of the $[\beta, f]$ error propagation analysis. As it has been concluded, the variance of m does not affect establishing the optimum number of clusters. An additional note is that the uncertainty of β and f, implicitly represented by varying m, does not affect establishing c_{opt}, either.

4. Results and Discussion

Fig. 10 shows the result of clustering. It was obtained using an in-house implementation of the FCM method. The horizontal axis of the diagram represents the angular range associated with one blade passage, corresponding to $360°/B = 72°$. The circular arc-shaped circumferential range at the blade tip radius has been rectified for an easier representation. Segments of the two neighbouring blades bounding the blade passage are drawn to the bottom of the figure for a lifelike explanation of the results. The angular position of the blades is determined by the angular encoder. $\beta = 0°$ is aligned with the tip TE of one certain blade, as illustrated on the sketch at the bottom of the figure. The blade LE, TE, and the blade tip is indicated with labels in the sketch. The circumferential extension of the projection of the blade tip region is realistically scaled (i.e. 45°). The blade motion is considered as being from the right to the left in the figure, as indicated in the sketch by an arrow. The vertical axis of the diagram represents the frequency range under evaluation. The $[\beta,\ f]$ data points (base sources) are indicated in the diagram by means of cross symbols. They are related to either of the $h = 1,\ 2,\ 3$ harmonic wave number values.

For $h = 2$ and 3, the angular difference is 36° and 24°, respectively, between the neighbouring base sources. The β angle and the central frequency f of the related Fourier component determine the position of each base source in the diagram (along the horizontal and vertical axis, respectively). The identified cluster centres, corresponding to $c_{\text{opt}} = 3$, are indicated in the diagram with diamonds. The clusters are labelled at their centres as Cluster 1, 2, and 3.

Each point of index i has c number of membership functions: $w_{i,1}, w_{i,2}, ...w_{i,c}$. In Fig. 10, the contour lines indicate the largest of those, $\max_j w_{i,j}$, that is the membership value of the point with respect to the closest cluster.

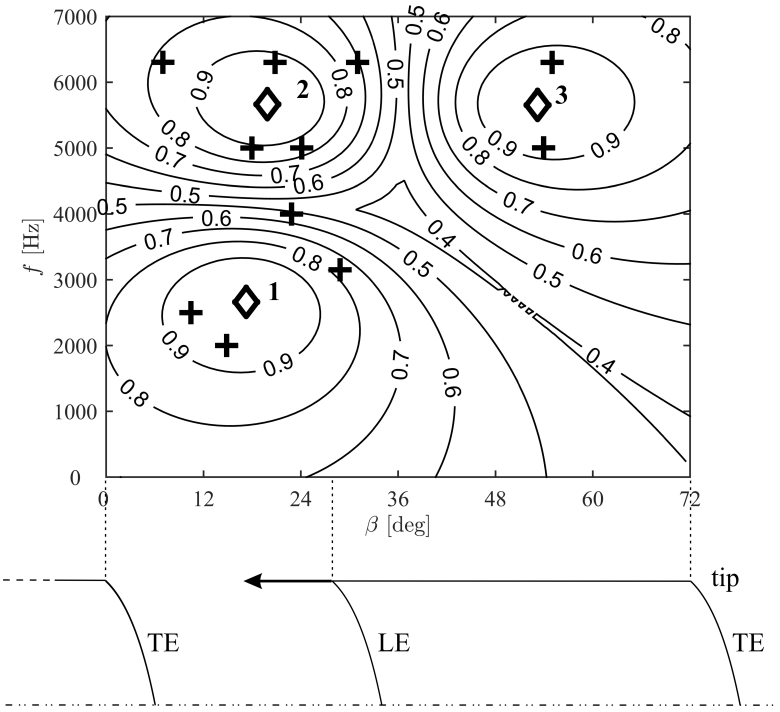

Figure 10: Representation and interpretation of the results of clustering. The scaled contour lines indicate the $w_{i,j}$ membership values corresponding to the closest cluster, the crosses are the base sources, while the diamonds show the cluster centres.

Comparing Fig. 8 to Fig. 10, the following conclusions can be drawn. The third-octave band peaks represent the narrowband maxima well, as they have

similar angular positions. The identified clusters 1 and 2 are also in agreement with the maximum locations, as most narrowband maxima fall into these peaks, with only a handful of them being localised elsewhere. No narrowband maximum falls into the area of Cluster 3, though. This means that there are no narrowband maxima in that region, and the identification of Cluster 3 is impossible by looking only at the maxima. It can only be found with the Fourier decomposition process, or by considering local maxima as well.

The present case study is taken as an illustrative example for evaluation of the results obtained from the algorithmic localisation method described herein. The discussion adds to the authors' previous work [8, 9, 10] from the following points of view. In the cited references, the identification of the noise sources was carried out for the same fan on an intuitive basis. The present evaluation takes the benefits of algorithmic localisation. It incorporates a systematic and comprehensive review of all noise sources possibly occurring in the same fan in the tip region. It is based on a quantitative comparison between characteristics derived from the measurements as well as those estimated from the semi-empirical aeroacoustic models established in reference [21]. The quantitative comparison is combined with a concerted analysis of the spectra (Figs. 3 and 7) and the cluster map (Fig. 10). Furthermore, the present discussion is supported by literature references, serving as basis for evaluating the observed qualitative trends.

For the quantitative comparison, the geometrical and aerodynamic data of the tip section, summarised in Table 4, have been taken as basis. These characteristics have been derived from the data available in [8, 9, 10]. For moderately loaded blades, reference [42] presents a clear distinction of the blade boundary layer and tip flow regions. Therefore, the use of the Lieblein diffusion factor D as blade loading indicator, correlating with the thickness of the blade boundary layer, has been judged reasonable in the tip region - even though the concept of D was originally applied to rectilinear, i.e. two-dimensional blade cascades [43]. This view is supported by the fact that such use of D is widespread in the analysis of three-dimensional axial fan rotor flows, also incorporating the vicin-

ity of the annulus walls (e.g. [44]). D, presented in Table 4, was considered for estimating the wake momentum thickness as $0.01\,C$, using Fig. 148 in [43]. A shape factor - i.e. displacement-to-momentum thickness ratio - of 1.4 has been assumed, as suggested in [45], and confirmed by the data in [46]. The above data enabled the estimation of the displacement thickness, presented in Table 4 as boundary layer thickness δ, being used in the semi-empirical aeroacoustic models.

Property	Dimension	Value
C	[mm]	130
θ_c	[°]	28
t	[mm]	1
γ	[°]	63
C/S_b	[-]	0.69
τ/C	[-]	0.053
W	[m/s]	23.2
α	[°]	2
Re	[-]	$2 \cdot 10^5$
Ma	[-]	0.07
D	[-]	0.4
δ	[mm]	2

Table 4: Characteristics at the rotor tip

Table 5 presents the characteristics of the aeroacoustic noise sources briefly estimated with use of the semi-empirical models published in reference [21]. As input to semi-empirical modelling, the data shown in Table 4 have been used. The calculations are based on the following parts of reference [21]. Profile vortex-shedding noise: Eqs. (53-60), Fig. 85. TBL – TE interaction noise: Eqs. (30-34), Fig. (78). Tip leakage flow noise (considering that τ/C in [42] is in fair agreement with the data in Table 4): Eqs. (61-65). Blunt TE vortex-shedding noise: Eq. (68), Figs. 95, 97. The table contains the estimated $\mathrm{Str}_{\mathrm{peak}}$ Strouhal

numbers related to the peak intensity associated with the various sources. The Strouhal number definitions incorporate various length scales and velocities for the various sources [21], which have been derived from the quantities in Table 4. With use of the aforementioned data, the f_{peak} frequencies related to the source peak intensities have been estimated, as shown in Table 5. The G gradient of drop of source intensity level, also incorporated in the table, has been obtained as follows. Lower and higher limiting frequencies have been approximated at which the source intensity drops by 10 dB relative to the peak value. G has been taken as the mean absolute value of the slope of the frequency-dependent source intensity curve within the range tailored by these limiting frequencies.

Aeroacoustic noise source	$\mathrm{Str}_{\mathrm{peak}}\,[-]$	$f_{\mathrm{peak}}\,[\mathrm{kHz}]$	$G\,[\mathrm{dB/kHz}]$	Cluster assigned
Profile vortex-shedding	0.2	2.3	12.6	–
TBL – TE interaction	0.1	1.2	8.6	1
Tip leakage flow	0.5	5.2	2.2	2, 3
Blunt TE vortex-shedding	0.2	4.6	9.7	–

Table 5: Model-based data

Using the data in Table 2, characteristics comparable with the "Model-based" data have been obtained for the three clusters, shown in Table 6. The peak intensity was estimated for each third-octave band of middle frequency f as follows, using the Component IDs in Table 2 as references in the explanation. For clusters 1 and 2, the a_f values related to the components "f / 0" and "f / 1 / 1" have been added. For Cluster 3, the a_f values related to the components "5000 / 0" and "5000 / 2 / 2", as well as "6300 / 0" and "6300 / 3 / 3", have been added. 20 times the logarithm of the ratio of the peak intensities estimated for the neighbouring third-octave bands resulted in characteristic drops of source intensity level. Dividing such drops by the difference between the middle frequencies resulted in representative G values. Within each cluster, f_{peak} has been established as the middle frequency of the third-octave band of highest calculated peak intensity. Further quantitative evaluation of the mea-

surement results will be necessary for consideration of the spatial and spectral distribution of absolute values of SSL. Such evaluation, offering a potential for refinement of semi-empirical aeroacoustic models, is a subject of future work.

Cluster ID	f_{peak} [kHz]	G [dB/kHz]
1	2.0	7.0
2	5.0	2.3
3	5.0	1.4

Table 6: Measurement-based data

In what follows, the possible dominance of the various noise sources, listed at the end of the Introduction, will systematically be discussed. As summary of the following discussion, the clusters are assigned to the relevant noise sources in the last column of Table 5. These results confirm the conclusions drawn on an intuitive basis in [8, 9, 10].

a) *Near-LE turbulence ingestion noise.* As references [22, 23] suggest, such noise occurs if the upstream turbulence impinges on the blade in the vicinity of the LE. Upstream turbulence is generated e.g. by means of a protection grille installed in front of the rotor. In the present case study, free inlet was provided to the rotor, i.e. no upstream turbulence was generated. On this basis, the occurrence of near-LE turbulence ingestion noise is excluded in the present case study.

b) *TBL noise.* The $D = 0.4$ value in Table 4 indicates moderate load for the blading under present investigation ([43, 24]). For moderately loaded blades, reference [15] concludes that noise generated on the blade surface due to boundary layer turbulence becomes less significant, and noise occurring near the TE dominates. This view is in accordance with reference [24] stating that the TBLs noise is usually less significant than the TBL – TE interaction noise. Fig. 10 suggests that the majority of the base sources locate out of the region of the blade chord along which the boundary layer develops. Therefore, the dominance of TBL noise is excluded for the presented case.

c) *Separated flow noise.* $D = 0.4$ indicates moderate blade load, i.e. stall-free operation [43, 24]. Therefore, the occurrence of separated flow noise is excluded in this case study.

d) *Profile vortex-shedding noise.* As illustrated in [24, 25], the signature of such noise appears as a remarkable peak in the spectra. Therefore, it is expected to be characterised by a relatively large G value. In Table 5, the model-based $f_{\text{peak}} = 2.3$ kHz value is in fair agreement with the measurement-based $f_{\text{peak}} = 2.0$ kHz data related to Cluster 1. However, the measurement-based $G = 7.0$ dB/kHz data for Cluster 1 is significantly below the model-based $G = 12.6$ dB/kHz value. The SPL spectrum in Fig. 3 does not present an outstanding peak near 2 kHz. Based on the above, profile vortex-shedding noise is considered as of minor importance in this case study.

e) *TBL – TE interaction noise.* As Table 5 presents, the model-based $f_{\text{peak}} = 1.2$ kHz value is near the measurement-based $f_{\text{peak}} = 2.0$ kHz data related to Cluster 1. It is noted here again that 2.0 kHz is a lower limit in the middle frequency of the third-octaves in the present evaluation of beamforming results. The measurement-based $G = 7.0$ dB/kHz data for Cluster 1 briefly agrees with the model-based $G = 8.6$ dB/kHz value. In the range of 1 to 4 kHz, the SPL spectrum in Fig. 3 is in qualitative agreement with the trends shown in [21, 23, 24] for turbulent boundary layer – TE interaction noise: a plateau-like range (with apparent local peaks) at lower frequencies, exhibiting a moderate, gradually increasing slope toward higher frequencies. In the cluster map in Fig. 10, the centre of Cluster 1 locates between the TE of the preceding blade and the LE of the adjacent blade. It is to be considered that the occurrence of near-LE turbulence ingestion noise has formerly been excluded. Therefore, Cluster 1 is to be assigned to the vicinity of the TE of the preceding blade. The above arguments support the view that *Cluster 1 represents the TBL – TE interaction noise generated by the preceding blade.*

f) *Tip leakage flow noise.* According to Table 5, the model-based $f_{\text{peak}} = 5.2$ kHz value is in fair agreement with the measurement-based $f_{\text{peak}} = 5.0$ kHz data related to Cluster 2. The measurement-based $G = 2.3$ dB/kHz data for

Cluster 2 also agrees with the model-based $G = 2.2$ dB/kHz value fairly well. These data are in accordance with the view in references [21, 42] that tip leakage flow noise is a high-frequency broadband noise. At 5 kHz, a break (starting point of a "hump") is slightly visible in the SSL spectrum (Fig. 7). Such qualitative feature also appears as a signature of tip leakage flow noise in [21, 47]. The slope of the SPL spectrum above 5 kHz is in fair agreement with the slope valid for the spectrum in [47] in the tip leakage flow noise-dominated range. As explained for Cluster 1, Cluster 2 also locates in the vicinity of the TE of the preceding blade, as indicated by the cluster map in Fig. 10. Based on [21, 23, 26], some part of the tip leakage flow noise can be interpreted as specific, concentrated TE noise sources. These arguments support the view that *Cluster 2 represents the tip leakage flow noise generated by the preceding blade.* In addition to the TBL – TE interaction noise represented by Cluster 1 , the tip leakage flow noise represented by Cluster 2 is also related, at least partly, to the TE [21, 23, 26]. The two noise mechanisms are linearly superimposed [21]. Consequently, Clusters 1 and 2 overlap both spatially as well as in the frequency domain. The cluster map in Fig. 10 shows that the centre of Cluster 2 locates at an angular position being approximately identical to that of the centre of Cluster 1. Furthermore, the base source at 4 kHz is nearly equally assigned to both clusters.

For Cluster 3, the related $f_{\text{peak}} = 5.0$ kHz and $G = 1.4$ data agree fairly well with the measurement-based data for Cluster 2, as well as with the model-based data for the tip leakage flow noise. This suggests that Cluster 3 represents a variety of tip leakage flow noise. However, its peculiarity is that its centre locates within the tip clearance region of the adjacent blade, i.e. downstream of the blade to which Cluster 2 has been assigned. The experimental and computational fluid dynamics studies in [8, 9, 10] support that the source related to Cluster 3 adds to the list of traditionally known noise classes presented in the Introduction. *Cluster 3 represents the double leakage flow noise.* Double-leakage occurs by such means that the tip leakage flow associated with Cluster 2 from noise generation point of view reaches

the pressure side at the tip region of the adjacent blade, and leaks across again [48].

g) *Blunt TE vortex-shedding noise.* As suggested by [23], the signature of such noise is a remarkable peak in the SPL spectrum. Therefore, it is expected to correspond to a relatively large G value. Table 5 presents model-based $G = 9.7$ dB/kHz and $f_{\text{peak}} = 4.6$ kHz values. For 5 kHz, the measurement-based G values are significantly below the model-based gradient. Neither the SPL nor the SSL spectrum shows any outstanding peak near 5 kHz. Therefore, blunt TE vortex-shedding noise is regarded as of minor importance in this case study.

5. Conclusions

A method has been proposed herein to localise and characterise blade-passage-periodic broadband aerodynamic noise sources in an axial fan, and to assign them to the underlying dominant aerodynamic phenomena. It is based on beamforming in a co-rotating system. A third-octave band evaluation of the beamforming results has been found as a suitable representation of the broadband sources. The method relies on the spatial Fourier expansion of the measured source strengths at a given radius. By such means, Fourier amplitude and phase spectra have been obtained for each third-octave band. The amplitude spectra enable the identification of significant Fourier components, by means of an algorithmic significance criterion. After a filtration process, the peaks related to the significant Fourier components have been retained as base sources. The localised noise sources, being extended both in space and in frequency, have been considered as clusters of the base sources obtained for the various bands. The FCM algorithm has been applied for clustering. The XB index has been involved as a robust means in determining the physically reasonable number of clusters, in an objective, algorithmic manner.

The proposed method offers the following advantages. By such means, it adds to the literature related to evaluation of beamforming results obtained for

axial fans.

- The method is algorithmised, being free from any subjective and arbitrary elements (such as visual inspection of beamform maps, and optics-based resolution criteria).
- A concerted quantitative evaluation of beamform data within multiple frequency bands is carried out.
- The Fourier analysis enables a filtration as well as detection enhancement technique. The removal of perturbations enhances the detectability of each significant blade-passage-periodic source.
- Thanks to the application of the XB index, the number of significant blade-passage-periodic sources can robustly be determined, without any a priori knowledge on the aerodynamic and aeroacoustic characteristics.
- The base sources originate from the Fourier analysis. As such, they are characterised by frequency, amplitude and angular position. The fuzzy clusters are characterised by middle frequency, and angular position of the cluster centre. Such straightforward quantification makes possible a convenient utilisation of the experimental results in refinements of semi-empirical aeroacoustic models.

For demonstrating the capabilities of the proposed method, an illustrative case study has been presented. The case study aimed at localising and characterising the significant broadband aeroacoustic noise sources in the tip region of a free-inlet, free-exhaust, rotor-only, low-speed fan rotor. The upstream-radiated noise has been recorded and processed by means of beamforming. The algorithmic method resulted in the localisation of three significant noise sources, represented in a cluster map. The paper reports on a systematic and comprehensive evaluation of the experimental results. All possible noise sources have been reviewed. Quantitative characteristics of the measured noise sources have been derived. They have been compared to data based on semi-empirical models set up in the literature for various noise sources. The measurement-based

spectra and the cluster map have been analysed in a concerted manner. The qualitative trends observed in the experimental results have been compared to those available in the literature. Based on the above, sources of TBL – TE interaction noise and tip leakage flow noise have been identified. The third source has been found as being different from the traditionally known noise classes. It has been identified as the source of double leakage flow noise.

The restrictions of the method proposed herein, besides the generally known limitations of frequency-domain beamforming (mutually incoherent monopole sources, and limits in spatial resolution at low frequencies), are the following. Only blade-passage-periodic sources are taken into account, therefore the effects of non-uniformity cannot be investigated. Furthermore, at least two clusters are to be considered in the data set for applicability of the XB index.

Acknowledgements

This work has been supported by the Hungarian National Research, Development and Innovation Centre under contracts No. K 112277 and K 119943.

The work relates to the scientific programs "Development of quality-oriented and harmonized R+D+I strategy and the functional model at BME" (Project ID: TÁMOP-4.2.1/B-09/1/KMR-2010-0002) and "Talent care and cultivation in the scientific workshops of BME" (Project ID: TÁMOP-4.2.2/B-10/1-2010-0009).

On behalf of B. Tóth, the project is supported by the ÚNKP-16-3-I. New National Excellence Program of the Ministry of Human Capacities.

References

[1] E. Canepa, A. Cattanei, F. M. Zecchin, G. Milanese, D. Parodi, An experimental investigation on the tip leakage noise in axial-flow fans with rotating shroud, Journal of Sound and Vibration 375 (2016) 115 – 131. doi:10.1016/j.jsv.2016.04.009.

[2] R. P. Dougherty, Beamforming in acoustic testing, in: T. J. Mueller (Ed.), Experimental Aeroacoustics, Springer, Berlin, 2002, pp. 62–97. doi:10.1007/978-3-662-05058-3.

[3] L. Koop, Beamforming in acoustic testing, in: M. L. Riethmuller, M. R. Lena (Eds.), VKI Experimental Aeroacoustics, von Kármán Institute for Fluid Dynamics, Rhode Saint Genese, 2006. doi:10.1007/978-3-662-05058-3.

[4] P. Sijtsma, S. Oerlemans, H. Holthusen, Location of rotating sources by phased array measurements, in: Proceedings of the 7$^{\text{th}}$ AIAA/CEAS Aeroacoustics Conference, Maastricht, 2001. doi:10.2514/6.2001-2167.

[5] G. Herold, E. Sarradj, Microphone array method for the characterization of rotating sound sources in axial fans, Noise Control Engineering Journal 63 (6) (2015) 546–551. doi:10.3397/1/376348.

[6] G. Herold, E. Sarradj, Frequency domain deconcolution for rotating sources on an axial fan (ID: BeBeC-2016-D18), in: Proceedings of the 6$^{\text{th}}$ Berlin Beamforming Conference, Berlin-Adlershof, 2016.

[7] O. Minck, N. Binder, O. Cherrier, L. Lamotte, V. Budinger, Fan noise analysis using a microphone array, in: International Conference on Fan Noise, Technology and Numerical Methods (Fan 2012), Senlis, 2012.

[8] T. Benedek, J. Vad, Study on the effect of inlet geometry on the noise of an axial fan, with involvement of the phased array microphone technique, Paper ID GT2016-57772, in: Proceedings of ASME Turbo Expo 2016, Seoul, 2016. doi:10.1115/GT2016-57772.

[9] T. Benedek, J. Vad, An industrial onsite methodology for combined acoustic-aerodynamic diagnostics of axial fans, involving the phased array microphone technique, International Journal of Aeroacoustics 15 (1-2) (2016) 81–102. doi:10.1177/1475472X16630849.

[10] T. Benedek, J. Vad, Spatially resolved acoustic and aerodynamic studies upstream and downstream of an industrial axial fan with involvement of the phased array microphone technique, in: Proc. 11th European Conference on Turbomachinery Fluid Dynamics and Thermodynamics, Madrid, Spain, 2015.

[11] C. Horváth, E. Envia, G. G. Podboy, Limitations of phased array beamforming in open rotor noise source imaging, AIAA Journal 52 (8) (2014) 1810–1817. doi:10.2514/1.J052952.

[12] C. Horváth, B. Tóth, P. Tóth, T. Benedek, J. Vad, Reevaluating noise sources appearing on the axis of beamform maps of rotating sources, in: International Conference on Fan Noise, Technology and Numerical Methods (Fan 2015), Lyon, 2015.

[13] R. P. Dougherty, R. C. Ramachandran, G. Raman, Deconvolution of sources in aeroacoustic images from phased microphone arrays using linear programming, International Journal of Aeroacoustics 12 (7&8) (2013) 699–718. doi:10.1260/1475-472X.12.7-8.699.

[14] J. Hald, Combined NAH and beamforming using the same array, in: B&K Technical Review 1, Brüel&Kjaer, 2005, pp. 11–39. doi:10.1016/0361-9230(84)90025-X.

[15] F. J. Zenger, G. Herold, S. Becker, E. Sarradj, Sound source localization on an axial fan at different operating points, Experiments in Fluids 57 (8) (2016) 136. doi:10.1007/s00348-016-2223-8.

[16] T. S. McKehnie, General Theory of Light Propagation and Imaging Through the Atmosphere, Springer, Cham Heidelberg New York Dordrecht London, 2016. doi:10.1007/978-3-319-18209-4.

[17] F. A. Jenkins, W. E. White, Fundamentals of Optics, 4th Edition Edition, McGraw-Hill Primis Custom Publishing, New York, 1976.

[18] D. F. Comesaña, K. Holland, E. Fernandez-Grande, Spatial resolution limits for the localization of noise sources using direct sound mapping, Journal of Sound and Vibration 375 (2016) 53–62. doi:10.1016/j.jsv.2016.04.010.

[19] B. Tóth, J. Vad, Fourier analysis of beamforming data at the tip of an axial fan rotor, Periodica Polytechnica, Mechanical Engineering 60 (3) (2016) 152–158. doi:10.3311/PPme.8935.

[20] B. Tóth, J. Vad, An efficient methodology for comprehensive evaluation of turbomachinery source maps (ID: BeBeC-2016-D15), in: Proceedings of the 6th Berlin Beamforming Conference, Berlin-Adlershof, 2016.

[21] T. F. Brooks, D. S. Pope, M. A. Marcolini, Airfoil self-noise and prediction, Tech. Rep. 1218, NASA Reference Publication (1989).

[22] J. K. Staubs, Real airfoil effects on leading edge noise, Ph.D. thesis, Virginia Polytechnic Institute and State University, Blacksburg, VA. (2008).

[23] M. Roger, S. Moreau, Extensions and limitations of analytical airfoil broadband noise models, International Journal of Aeroacoustics 9 (3) (2010) 273–305. doi:10.1260/1475-472X.9.3.273.

[24] T. Carolus, Ventilatoren, Vieweg+Teubner Verlag, Viesbaden, 2003. doi:10.1007/978-3-8348-2472-1.

[25] S. Yarusevych, M. Boutilier, Vortex shedding characteristics of a NACA 0018 airfoil at low Reynolds numbers, AIAA Paper 2010-4628, in: Proceedings of the 40th Fluid Dynamics Conference and Exhibit, Chicago, IL, 2010. doi:10.2514/6.2010-4628.

[26] M. C. Jacob, J. Grilliat, R. Camussi, G. C. Gennaro, Aeroacoustic investigation of a single airfoil tip leakage flow, International Journal of Aeroacoustics 9 (3) (2010) 253–272. doi:10.1260/1475-472X.9.3.253.

[27] C. Lowis, P. Joseph, Determining the strength of rotating broadband sources in ducts by inverse methods, Journal of Sound and Vibration 295 (3) (2006) 614–632. doi:10.1016/j.jsv.2006.01.031.

[28] W. Pannert, C. Maier, Rotating beamforming–motion-compensation in the frequency domain and application of high-resolution beamforming algorithms, Journal of Sound and Vibration 333 (7) (2014) 1899–1912. doi:10.1016/j.jsv.2013.11.031.

[29] J. C. Bezdek, R. Ehrlich, W. Full, FCM: The fuzzy c-means clustering algorithm, Computers & Geosciences 10 (2-3) (1984) 191–203. doi:10.1016/0098-3004(84)90020-7.

[30] N. R. Pal, J. C. Bezdek, On cluster validity for the Fuzzy c-Means model, IEEE Transactions on Fuzzy Systems 3 (3) (1995) 370–379. doi:10.1109/91.413225.

[31] H. Zhang, X. Chen, Z. Du, X. Li, R. Yan, Nonlocal sparse model with adaptive structural clustering for feature extraction of aero-engine bearings, Journal of Sound and Vibration 368 (2016) 223 – 248. doi:10.1016/j.jsv.2016.01.017.

[32] J. Suckling, T. Sigmundsson, K. Greenwood, E. T. Bullmore, A modified fuzzy clustering algorithm for operator independent brain tissue classification of dual echo MR images, Magnetic Resonance Imaging 17 (7) (1999) 1065–1076. doi:10.1016/S0730-725X(99)00055-7.

[33] A. W.-C. Liew, H. Yan, An adaptive spatial fuzzy clustering algorithm for 3-D MR image segmentation, IEEE Transactions on Medical Imaging 22 (9) (2003) 1063–1075. doi:10.1109/TMI.2003.816956.

[34] M. Kühne, R. Togneri, S. Nordholm, Robust source localization in reverberant environments based on weighted fuzzy clustering, IEEE Signal Processing Letters 16 (2) (2009) 85–88. doi:10.1109/LSP.2008.2009833.

[35] F. J. Huera-Huarte, A. Vernet, Vortex modes in the wake of an oscillating long flexible cylinder combining POD and fuzzy clustering, Experiments in Fluids 48 (6) (2010) 999–1013. doi:10.1007/s00348-009-0786-3.

[36] A. Vernet, G. A. Kopp, Classification of turbulent flow patterns with fuzzy clustering, Engineering Applications of Artificial Intelligence 15 (3) (2002) 315–326. doi:10.1016/S0952-1976(02)00037-4.

[37] A. Van Hirtum, D. Berckmans, Fuzzy approach for improved recognition of citric acid induced piglet coughing from continuous registration, Journal of Sound and Vibration 266 (3) (2003) 677–686. doi:10.1016/S0022-460X(03)00593-5.

[38] G. Barkó, J. Abonyi, J. Hlavay, Application of fuzzy clustering and piezoelectric chemical sensor array for investigation on organic compounds, Analytica Chimica Acta 398 (2) (1999) 219–226. doi:10.1016/S0003-2670(99)00377-3.

[39] W. Wang, Y. Zhang, On fuzzy cluster validity indices, Fuzzy Sets and Systems 158 (19) (2007) 2095–2117. doi:10.1016/j.fss.2007.03.004.

[40] B. Balaskó, A. János, B. Feil, A MATLAB toolbox and its web based variant for fuzzy cluster analysis, in: 7^{th} International Symposium of Hungarian Researchers on Computational Intelligence, Budapest, 2006.

[41] X. L. Xie, G. Beni, A validity measure for fuzzy clustering, IEEE Transactions on Pattern Analysis and Machine Intelligence 13 (8) (1991) 841–847. doi:10.1109/34.85677.

[42] T. F. Brooks, M. A. Marcolini, Airfoil tip vortex formation noise, AIAA Journal 24 (2) (1986) 246–252. doi:10.2514/3.9252.

[43] S. Lieblein, Experimental flow in two-dimensional cascades, Chapter VI in Aerodynamic Design of Axial-Flow Compressors", Tech. Rep. SP-36, NACA, Washington, DC (1965).

[44] A. Corsini, F. Rispoli, Using sweep to extend the stall-free operational range in axial fan rotors, Proc. Instn. Mech. Engs, Part A: J. Power and Energy 218 (3) (2004) 129–140. doi:10.1243/095765004323049869.

[45] H. Schlichting, Boundary-layer Theory, 7th Edition, McGraw-Hill, New York, 1979.

[46] T. F. Brooks, M. A. Marcolini, Scaling of airfoil self-noise using measured flow parameters, AIAA Journal 23 (2) (1985) 207–213. doi:10.2514/3.8896.

[47] B. Bizjan, M. Milavec, B. Širok, F. Trenc, M. Hočevar, Energy dissipation in the blade tip region of an axial fan, Journal of Sound and Vibration 382 (2016) 63–72. doi:10.1016/j.jsv.2016.06.036.

[48] S. A. Khalid, A. S. Khalsa, I. A. Waitz, C. S. Tan, E. M. Greitzer, J. J. Cumpsty, N. A. amd Adamczyk, F. E. Marble, Endwall blockage in axial compressors, Journal of Turbomachinery 121 (1999) 499–509. doi:10.1115/1.2841344.